RESEARCH ARTICLE

NANO · MICRO small
www.small-journal.com

Construction of Nickel Molybdenum Sulfide/Black Phosphorous 3D Hierarchical Structure Toward High Performance Supercapacitor Electrodes

Mansi Pathak, Pratap Mane, Brahmananda Chakraborty, Jung Sang Cho, Sang Mun Jeong,* and Chandra Sekhar Rout**

Supercapacitors (SCs) with outstanding versatility have a lot of potential applications in next-generation electronics. However, their practical uses are limited by their short working potential window and ultralow-specific capacity. Herein, the facile one-step in-situ hydrothermal synthesis is employed for the construction of a $NiMo_3S_4$/BP (black phosphorous) hybrid with a 3D hierarchical structure. After optimization, the $NiMo_3S_4$/BP hybrid displays a high specific capacitance of 830 F/g at 1 A/g compared to the pristine $NiMo_3S_4$ electrode. The fabricated $NiMo_3S_4$/BP//$NiCo_2S_4$ /Ti_3C_2Tx asymmetric supercapacitor exhibits a better specific capacitance of 120 F/g at 0.5 A/g, which also demonstrates a high energy density of 54 Wh/kg at 1148.53 W/kg and good cycle stability with capacity retention of 86% and 97% of Coulombic efficiency after 6000 cycles. Further from the DFT simulations, the hybrid $NiMo_3S_4$/BP structure shows higher conductivity and quantum capacitance, which demonstrate greater charge storage capability, due to enhanced electronic states near the Fermi level. The lower diffusion energy barrier for the electrolyte K_+ ions in the hybrid structure is facilitated by improved charge transfer performance for the hybrid $NiMo_3S_4$/BP. This work highlights the potential significance of hybrid nanoarchitectonics and compositional tunability as an emerging method for improving the charge storage capabilities of active electrodes.

1. Introduction

Implementing an economy with a reduced carbon footprint and environmental impact has been the subject of extensive research throughout the years. Utilizing less conventional power sources is necessary to achieve energy harvesting. Notwithstanding the significant improvements in energy generation, storage, and communication brought about by contemporary technology and research, new discoveries are always being made to further optimize and manage these processes. Effective energy-storage systems are extremely desirable because power sources are always needed. In order to address the problems with the charge storage mechanism, energy storage technology is now focusing on developing hybrid supercapacitors.[1–4] Regardless, the primary barrier to supercapacitors' (SCs) broad range of applications is their comparatively low energy density. Thus, the primary obstacle to effectively employing supercapacitors is to increase their

M. Pathak, C. S. Rout
Centre for Nano and Material Sciences
Jain (deemed-to-be University)
Jain Global Campus
Kanakapura Road, Bangalore 562112, India
E-mail: r.chandrasekhar@jainuniversity.ac.in

P. Mane
Seismology Division
Bhabha Atomic Research Centre
Trombay, Mumbai 400085, India

B. Chakraborty
High Pressure and Synchrotron Radiation Physics Division
Bhabha Atomic Research Centre
Trombay, Mumbai 400085, India
E-mail: brahma@barc.gov.in

B. Chakraborty
Homi Bhabha National Institute
Mumbai 400094, India

J. S. Cho
Department of Engineering Chemistry
Chungbuk National University
Cheongju, Chungbuk 28644, Republic of Korea

S. M. Jeong, C. S. Rout
Department of Chemical Engineering
Chungbuk National University
Cheongju, Chungbuk 28644, Republic of Korea
E-mail: smjeong@chungbuk.ac.kr

The ORCID identification number(s) for the author(s) of this article can be found under https://doi.org/10.1002/smll.202310120

DOI: 10.1002/smll.202310120

energy density without compromising any of their additional capacitive characteristics. Based on the charge storage mechanism, supercapacitors known as electrochemical double-layer capacitors (EDLCs) are double-layer capacitances produced at the electrode/electrolyte interface by the adsorption of electrolyte ions. A device that implements a different mechanism, containing a faradic-type electron transfer interaction between the electrode/electrolyte interface, is termed a pseudocapacitive (PC) or redox type supercapacitor.[5,6] The specific problems include low power density in batteries and low energy density in SCs. Hybrid supercapacitors belong to a distinctive category of devices that jointly rely on the electrostatic and electrochemical phenomena; that is, they have two types of working electrodes: one is capacitive and the other is battery-type. The elevated power density and energy density are provided by the synergistic electrode mechanisms, which further expand a broad variety of potential windows.[7–10]

Ternary transition metal sulfides (TMS) are emerging as a viable new electrode material for SCs owing to their higher conductivity and strong electrochemical activity, particularly compared to metal oxide materials that have been extensively explored. This is because a variety of electrode materials for SCs are now available.[11–13] However, given its fascinating electrochemical characteristics, bare TMS by itself frequently experiences poor specific capacitance. It is recommended that a fresh approach be put out to raise the specific capacity of TMS electrode materials in order to solve this problem.[14,15] Presently, considering the limited practicality of the active material and high charge transfer resistance, the practical specific capacity of TMS is quite minuscule when compared to theoretical values. The spinel-type $NiCo_2S_4$ is one of the TMS materials that has been studied in great detail for SCs because of its high theoretical capacitance, easy synthesis, low cost, and widespread availability. On the other hand, there are only reports on $NiMo_3S_4$ batteries with SCs that are hierarchical.[16–18] However, there is a risk of low cycle stability when using these bimetallic sulfides alone as an electrode material. Therefore, studies on bimetallic TMS-based composites are being conducted in an effort to improve their electrochemical performance. According to recent studies, the proper design and selection of TMS with different kinds of composites can increase redox processes by increasing specific capacitance through the synergistic impact of many mechanisms.[19,20] Considering their multiple oxidation states, reversible redox behavior, and affordability, Ni–Mo-based chalcogenides, among transition metal chalcogenides; TMCs, offer potential for application in supercapacitors. Particularly, Mo facilitates electrical conductivity; while, Ni-ions primarily distribute high specific capacitance in Ni–Mo-based chalcogenides. Further, the long-term robustness of the electrodes is enhanced by Mo's corrosion-resisting attributes.[21–23] In comparison to S and O-based TM chalcogenides, Se-based TM chalcogenides have a higher degree of covalency and semiconducting characteristics due to the chalcogen with electronegativity that follows a hierarchy of Se < S < O. Chalcogens improve the electrochemical performance of the supercapacitor by enhancing the charge transfer characteristics of TM chalcogenide-based electrode materials in electrode/electrolyte interfaces by promoting electrolytic diffusion with rapid redox reactions.[24,25]

However, during the high-temperature synthesis methods, agglomeration of TM chalcogenides and a subsequent reduction in the number of catalytically active sites are often the result of inadequate structuring of TM chalcogenide nanostructures. This means that in order to get the best electrocatalytic performance of TM chalcogenides, hierarchical 2D nanoarchitecture, including a few numbers of irregular defects, can be preferred.[26,27] The previous investigations suggest that a metal sulfide doping technique that tunes the nanostructure with a hierarchical design may be useful for energy-related applications. Recently, for catalysts Ni–Mo–S-based composites and hybrids[18,28,29] have been investigated for various energy-related applications; the results show excellent stability and strong catalytic activity. Moreover, effective substitution of electron donors into 2D nanostructures has been reported to produce distinct surface dipoles, which might lead to increased chemical reactivity as well as stabilize metastable surface structures.[30,31] Consequently, due to their better electrical conductivity and catalytic activity, Ni–Mo–S-based hybrid electrodes are anticipated to be the best electrodes for SCs. The primary challenge associated with TMS is their tendency to self-agglomerate, which hinders ion transport and reduces the number of electrochemically active sites.[22,32,33]

Recently, the class of 2D materials has been enlarged with the advent of 2D black phosphorus (BP), an exceptionally thermodynamically inert phosphorus allotrope. In addition to its good carrier mobility, huge surface area, and adaptable band gap, BP has been the subject of intensive research over the past few years as a p-type direct band gap semiconductor layered material. A broad spectrum of applications, including energy storage, solar cells, sensors, photovoltaic devices, and heterojunction p–n diodes, have been investigated for BP based on these inherent features.[34–36] Further, because of its better mechanical flexibility, 2D BP constitutes a viable approach for flexible devices. Taking into account the significance of BP, Liang et al.[37] examined the HER activity of MoS_2/BP. The MoS_2/BP heterostructure with several active sites and functional interfaces that demonstrated notable HER catalytic efficiency was found in their study. From our group, Radhakrishnan et al.[38] have synthesized an n–p-type MoS_2/BP heterostructure using a simple hydrothermal method, to address this slow the electrochemical activity and have tested its electrochemical performance for the first time. For the further investigation of electrochemical capabilities, an all-solid-state asymmetric supercapacitor was built, using VS_2/BP for the positive electrode and MoS_2/BP for the negative electrode. With an energy density of 34.71 Wh kg^{-1} at 4031 W kg^{-1} of power density and a capacitance of ≈114 F g^{-1}, the suggested all-phosphorene-based device showed remarkable cycle stability and capacitance retention. Further, the studies suggest that constructing an asymmetric supercapacitor (ASC) device is another practical method for improving the electrochemical characteristics of the supercapacitor device. A battery-like electrode can be employed to achieve high energy density in the construction of the ASC device; while, an EDLC-type electrode can be used to yield high power density. In contrast to symmetrical supercapacitors, the ASC device that uses an aqueous electrolyte has a working potential that is higher than the breakdown potential for the electrolysis.[39,40]

Perceiving the aforementioned advantages, here, we construct a hierarchical $NiMo_3S_4$ nanosheet with plenty of exposed

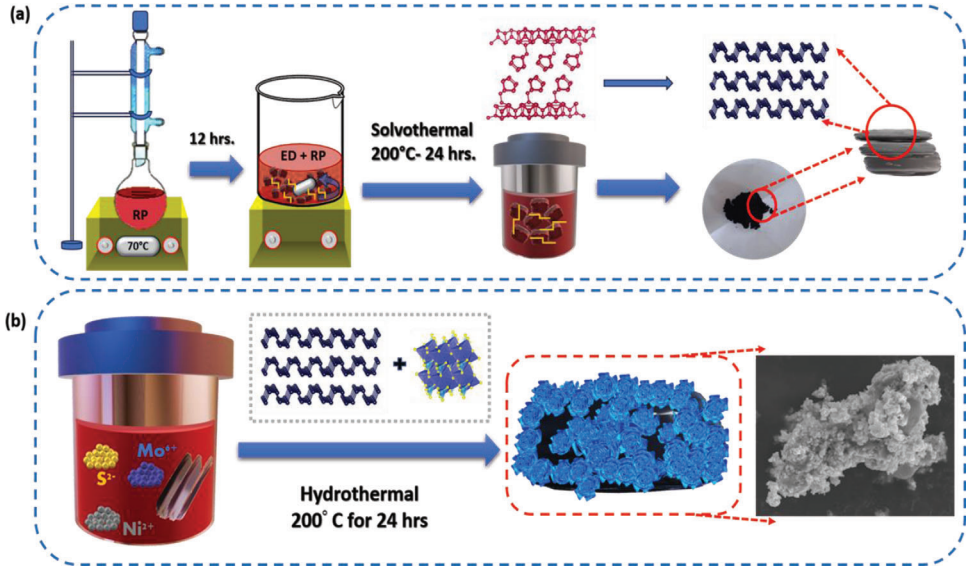

Figure 1. Schematic depiction of composite formation: a) synthesis of BP from RP; b) synthesis of NMS/BP via a simple hydrothermal method.

active sites and edges on 2D black phosphorus sheets (referred to as $NiMo_3S_4$/BP) for high-performance asymmetric supercapacitors. There are several benefits to this novel 3D hierarchical system for enhanced energy storage. A straightforward one-step in situ hydrothermal synthesis is implemented in this case to synthesize a 3D hierarchical $NiMo_3S_4$/BP hybrid. Additional support is provided that improves redox active sites for electrochemical reactions in addition to supporting the BP and being embedded by $NiMo_3S_4$. This aids in preventing self-stacking in many ion transfer channels. When compared to a pure $NiMo_3S_4$ (NMS)electrode, the $NiMo_3S_4$/BP (NMS/BP) hybrid exhibits a high specific capacitance capacity of 830 F g^{-1} at 1 A g^{-1} following optimization. Better specific capacitance of 120 F g^{-1} at 0.5 A g^{-1} and high energy density of 54 Wh kg^{-1} at 1148.53 W kg^{-1} are two features of the constructed $NiMo_3S_4$/BP//$NiCo_2S_4$@$Ti_3C_2T_x$ asymmetric supercapacitor that show good cycle stability with capacity retention of 86% and 97% of Coulombic efficiency after 6000 cycles. Sufficient electrochemical performances of the $NiMo_3S_4$/BP hybrid demonstrate the possible applications of supercapacitors. DFT studies serve to theoretically analyze and validate the experimental results. We simulate density functional theory and give the structural and electrical characteristics of NMS and its BP-doped hybrid NMS/BP to validate experimental results. The hybrid structure NMS/BP exhibits an elevation in electronic states close to the Fermi level as a result of charge transfer from BP's P 3p orbital Mo 4d orbital of NMS. The improvement in conductivity and quantum capacitance that result in the hybrid structure's higher charge storage ability might be attributed to this improvement in electronic states. The enhanced charge transfer performance for the hybrid NMS/BP, as seen in the experiment, is responsible for the decreased diffusion energy barrier for the electrolyte K+ ions in the hybrid structure. The potential importance of compositional tunability and hybrid nano architectonics as a developing technique for enhancing the active capacity of electrodes to store charges is highlighted in the present work.

2. Results and Discussion

2.1. In Situ Growth Mechanism of $NiMo_3S_4$/BP

The stepwise synthesis procedure is illustrated in **Figure 1b**. The BP and NMS/BP ($NiMo_3S_4$/BP) hybrid formation process is shown in Figure 1. The BP is synthesized via a two-step solvothermal process; similar to the report from Wang et al.[42] on low-temperature liquid phase synthesis of BP from (Red phosphorous) RP employing (ethylene diamine) ED, a commercial low-toxicity solvent is reported. Here, we employ a modified synthesis approach. The two-step BP synthesis begins with RP reflux at 70 °C in an oil bath. This reflux process removes RP surface oxygen. The detailed discussion on the crystallization of BP from RP is explained in our previous report by Radhakrishnan et al.[38]

The hydrothermal procedure for forming $NiMo_3S_4$ nanosheet architecture involves chemical reactions such as a possible pathway involving $(NH_4)_6Mo_7O_{24}.4H_2O$ disintegration, reduction, and sulfidation,[41] revealed by Equations (1)–(5) as follows:

$$(NH_4)_6Mo_7O_{24}.4H_2O + 3H_2O \rightarrow 7\,MoO_3 + 6NH_3.\,H_2O \quad (1)$$

$$Na_2MoO_4.2H_2O + 3H_2O \rightarrow MoO_4^{2-} + 2\,Na^+ + 2H_2O \quad (2)$$

$$C_2H_5NS + 2H_2O \rightarrow NH_3 + 2CO_2 + H_2S + 2H^+ \quad (3)$$

$$H_2O + H_2S \rightarrow HS^- + H_3O^+ \quad (4)$$

$$6\,HS^- + 10H_3O^+ + Ni_2^+ + 3MoO_4^{2-} \rightarrow NiMo_3S_4 + 18H_2O + 2SO_2 \quad (5)$$

The $NiMo_3S_4$ (NMS) hierarchy is formed in three steps: Sulfur precursor thioacetamide dissociates and interacts with water to form H_2S, CO_2, and NH_3. To felicitate the growth of NMS nanosheets architecture on 2D BP nanosheets, the sulfur component in the first step combines with water and dissociates into HS^- and H_3O^+ ions. These ions interact with ionized precursors of Ni and Mo materials in growth solution.[13,18]

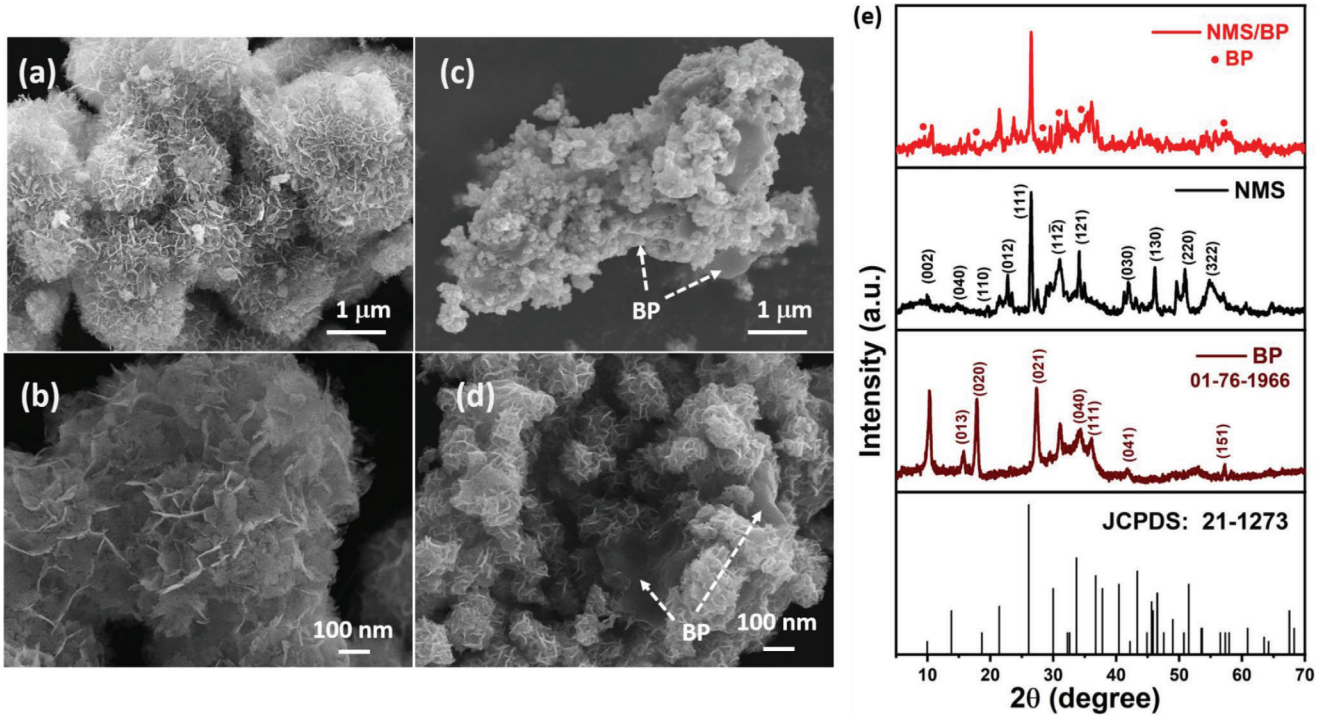

Figure 2. FESEM images of a,b) NMS; c,d) NMS/BP at different magnifications. e) XRD analysis of NMS and NMS/BP hybrid.

2.2. Morphological, Structural, and Compositional Analysis of $NiMo_3S_4$ and $NiMo_3S_4$/BP

As-prepared NMS and NMS/BP hybrid is confirmed using FESEM and TEM for structural morphology. A stack of FESEM micrographs is shown in **Figure 2**. In Figure 2a,b, FESEM images of pristine NMS at various magnifications reveal the well-defined flower-like structure grown spherically by a coverage of the ultrathin nanosheets surface forming bundles NMS nanoflowers. Unlike traditional carbon materials, BP also partakes a 2D nanosheet structure that provides a conductive platform for active materials to fill void spaces and enhance conducting channels for electron transport. In particular, the clusters have a layering arrangement with a homogeneous distribution similar to an orthorhombic BP.[38] As shown in Figure S1a,b, Supporting Information, the crumbled thick sheets of BP architecture with many channels provide double-layer capacitance and huge surface area. Figure 2c,d gives the morphological detail of $NiMo_3S_4$ nanosheets on accessible BP surface implemented for constructing 3D hierarchical nanosheet arrays through hydrothermal growth and post-annealing. Adsorption of anions on $NiMo_3S_4$ surfaces stimulates nano-crystal development and builds 3D hierarchical nanosheet arrangements during hydrothermal processing.[18] High-magnification photographs of BP with NMS nanosheets exhibit a nanostructure with several, extremely thin nanosheets growing vertically over the BP surface. $NiMo_3S_4$ nanosheet arrays consistently grown on exposed BP surfaces contribute to expansive channels for fast electrochemical response, thereby offering electrolytic ions with a large area to proceed. As shown in high magnification FESEM micrograph, a firm contact in NMS/BP hybrid nanostructure indicates the stability of the material and structural integrity during electrochemical processes.

The crystalline arrangement and phase uniformity are determined by XRD data. Figure 2e compares the pristine $NiMo_3S_4$ nanosheets and $NiMo_3S_4$/BP hybrids X-ray diffractograms. BP exhibits characteristic peaks at 17.43°, 27.54°, 34.38°, 35.52°, 41.2°, and 57.65°, which confirm the presence of BP and are consistent with the JCPDS file number 073–1358. Here, the magnitude of the (020) peak of BP at ≈17° is expanded; while, the RP peak at ≈15.2° is diminished (Figure S1c).[38] This suggests that the RP component in the sample is extremely minimal and that BP is effectively synthesized. The diffraction peaks at 10.29°, 14.56°,19.2°, 22.5°, 26.34°, 31.9°, 34.22°, 41.6°, 46.30°, 50.75°, and 54.5° are indexed to the (002), (040), (012), (100), (111), (11-2), (121), (030), (130), (220), and (322) planes, respectively, exhibiting $NiMo_3S_4$ triclinic transition phase of space group (JCPDS card no. 21–1273).[43,44] Potential secondary phases such as MoS_2 and NiS_2 are not observed. The exhibiting $NiMo_3S_4$ triclinic phase is identical to the basic Chevrel-type Mo_3S_4 phase (ICSD: 237587)[45] which further approves the $NiMo_3S_4$ phase is successfully formed. The possible method for making flower-like $NiMo_3S_4$ nanostructures via the hydrothermal route is explained in the Experimental Section. The following is the possible mechanism of the formation of $NiMo_3S_4$ crystal transformation into the $\bar{P}1$ triclinic space group. Three distinct Mo^{2+} sites are not identical. The Mo^{2+} site initially establishes coordination with five S^{2-} atoms, leading to the creation of a squared pyramidal structure with four vertices, thereby forming MoS_5. This arrangement comprises three identical NiS_4 tetrahedra, five edges, and one interaction between two edges. The Mo^{2+} site bonds to five S^{2-} atoms to generate MoS_5 square pyramids, which share

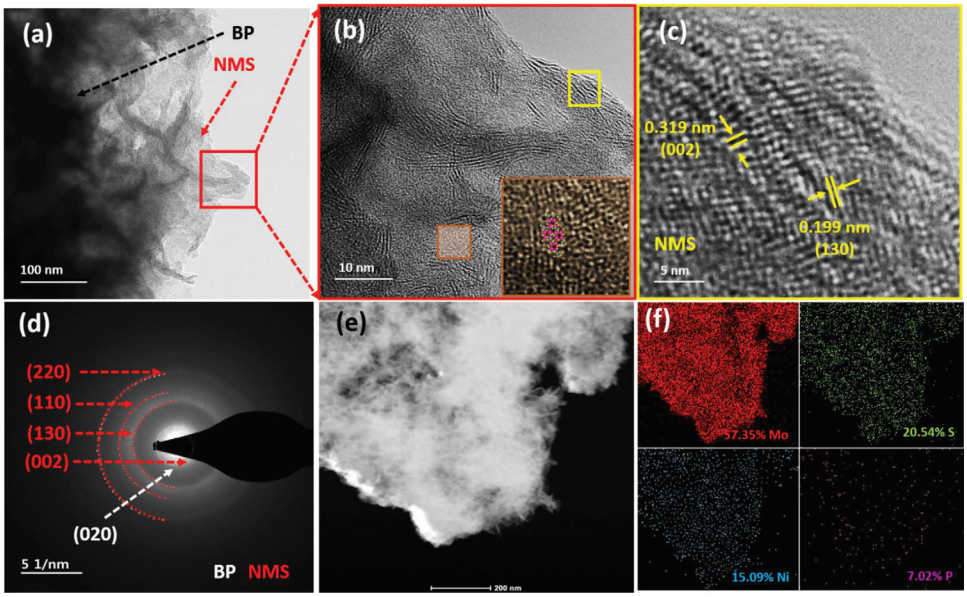

Figure 3. a) TEM image of $NiMo_3S_4$/BP; b,c) HR-TEM images of $NiMo_3S_4$/BP; d) SAED pattern; red- $NiMo_3S_4$ and white-BP; and e) HAADF-STEM with EDS mapping analysis.

corners with four MoS_5 pyramids, corners with five comparable NiS_4 tetrahedra, and edges with five MoS_5 pyramids. Ni^{2+} bonds to four S^{2-} atoms to create deformed NiS_4 tetrahedra with twelve MoS_5 square pyramids, one edge-edge, and one NiS_4 tetrahedra. Four S^{2-} sites are inequivalent. The first S^{2-} site bonds S^{2-} in a five-coordinate geometry to four Mo^{2+} and one Ni^{2+} atoms. The second S^{2-} site bonds four Mo^{2+} atoms in a four-coordinate geometry. S^{2-} is bound using a five-coordinate geometry to three Mo^{2+} and two equivalent Ni^{2+} atoms in the third location. S^{2-} is linked in a five-coordinate geometry to four Mo^{2+} and one Ni^{2+} atom in the final position.[43] At ≈17.44°, the strength of the (020) peak of BP develops; while, the RP peak at 15.2° declines, showing that the compounds RP concentration is low and that BP is produced. The BP reflection peaks at ≈30° may be caused by two P atoms being replaced by O or H atoms or a periodic distortion or stacking defect in the *c*-direction of crystal structure.[39]

The inherent morphological characteristics of $NiMo_3S_4$/BP hybrid nanostructure are examined through TEM, HR-TEM, and HAADF-STEM with EDS, as shown in **Figure 3**. $NiMo_3S_4$ nanosheets have expansive, uniform sheets or flakey channels morphology, indicating ultrathin, defect-free arrangements of the crystals. The morphological and crystallographic orientation of the $NiMo_3S_4$/BP samples were confirmed by the low and high magnification TEM analysis. Figure 3a displays the TEM image of $NiMo_3S_4$/BP, (Figure 3b,c) HR-TEM of $NiMo_3S_4$/BP (inset- hierarchical Ni–Mo–S arrangements of crystal in $NiMo_3S_4$ nanosheets), wherein the flakes on $NiMo_3S_4$ are seen to be decorated over BP sheet. The lattice spacing of 0.319 and 199 0.199 nm confirms the (200) and (310) planes of $NiMo_3S_4$. The SAED pattern (Figure 3d) shows polycrystalline nature wherein pattern marked in RED outline shows NMS and white outline assigns to (020) plane of BP. HAADF-STEM with EDS mapping analysis (Figure 3e) confirms the homogenous distribution of components such as Ni, Mo, and S, indicating that O^{2-} is replaced by S^{2-} during the anion-exchange process.[46] STEM-EDS mapping reveals a homogeneous distribution of components Ni (blue), Mo (red), S (green), and P (purple) in the hybrid architectures (Figure 3f). The BP structures serve as a backbone for hierarchical $NiMo_3S_4$/BP hybrid construction. The ultra-high surface area of the BP layer reduces the stacking of $NiMo_3S_4$ nanosheets during the in situ growth process, improving electron transport kinetics due to strong electrical conductivity. The one-step in situ hydrothermal synthesis approach enhances electrocatalytic capability and stability in hybrid matrices by sulfurizing without additive impurities during the electrochemical investigations.

The chemical composition and elemental phases of the $NiMo_3S_4$/BP sample are examined by X-ray photoelectron spectroscopy (XPS) analysis. Figure S2a–c, Supporting Information shows that the $NiMo_3S_4$/BP sample contains just Ni, Mo, S, P, O, and C, as confirmed by STEM-EDS and XRD data. The high-resolution XPS spectra of Mo 3d illustrated in **Figure 4a** reveals two significant peaks at 229.4 and 232.2 eV, indicating the predominant role of Mo^{4+} in $NiMo_3S_4$/BP. In addition to the Mo^{4+} $3d_{5/2}$ signal, an indistinct peak at 226.2 eV is instigated by the S 2s orbital. Higher binding energy doublet peaks of Mo $3d_{5/2}$, 232.9 eV and Mo $3d_{3/2}$, 235.9 eV may indicate the Mo^{4+} oxidation state, presumably due to insufficient reduction in the MoO_4^{2-} species during the hydrothermal synthesis progression, and the peaks at 238 eV shows Mo—O—P bonding, respectively.[18,38] The peaks at 856.3 and 874.3 eV in the high-resolution XPS spectra of $NiMo_3S_4$/BP as shown in Figure 4b correspond to Ni $2p_{3/2}$ and Ni $2p_{1/2}$, respectively; whereas, Ni satellite peaks at 860.1 and 879.6 eV may be identified. A minuscule peak at 852.6 eV is correlated to the Ni 2p signal from the Ni^{2+}. The binding energies of the six prominent peaks in Figure 4c (161.9, 163.1, 163.8, 165.1, 168.5, and 169.6 eV) correspond to $S2p_{3/2}$, $S2p_{1/2}$, and SO_4^{2-}, respectively. The S $2p_{3/2}$ (≈163.57 eV) and S $2p_{1/2}$ (≈164.51 eV) peaks accompanying the broad satellite represent the existence of the S^{2-} state. In Figure 4d, the P 2p two peaks at 133.6 and 135 eV are attributed to P_2O_5 bonding, indicating that the

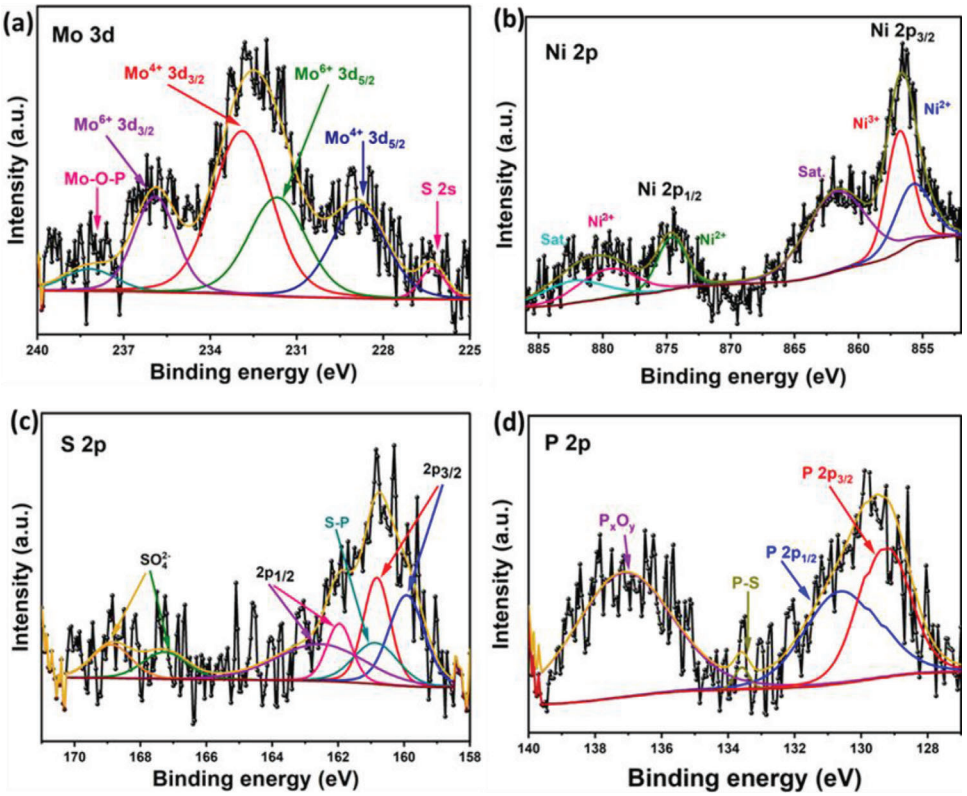

Figure 4. High-resolution XPS spectra of $NiMo_3S_4$/BP. a) Mo 3d; b) Ni 2p; c) S 2p; and d) P 2p.

surface of the BP is slightly oxidized. The Peak at 133.3 eV presents P—S bonding.[16–18] Studies have suggested that easily adjustable valence states in nickel can boost the faradaic capacity of active material whereas Mo ions can increase electronic conductivity. The high-resolution C 1s spectra (Figure S2b, Supporting Information) reveal carbon bond energies of 284.6 eV (C—C), 285.5 eV (C═C), and 286.6 eV (C—O). In Figure S2c, Supporting Information, the O 1s spectrum displays three peaks at 529.98, 531.41, and 533.70 eV, representing lattice oxygen, including M—O bonding, OH— ions, and adsorbed water molecules. Oxidized surfaces may contain OH^- groups, as shown by O 1s spectra, and oxygen species cannot be fully ruled out.[47] The lone-pair electron in the P atom enables BP oxidization to be readily available and hybrid structure formation to be feasible. Thus, P—O and Mo—O species interact in the nanocomposite and together form Mo—O—P. Though the same species has been observed in the P 2p and Mo 3d spectra, the peak at 533 and 531.6 eV in Figure S2c, Supporting Information indicates Mo—O—P bonds.[38] XPS suggests that NMS/BP hybrid structure origins substantially change its electronic structure and accelerate electron transport, improving energy storage performance. Specifically, the NMS/BP hybrid demonstrates a higher BET surface area and a considerably greater pore volume (26.103 $m^2\ g^{-1}$; 0.0908 $cm^3\ g^{-1}$) compared to pristine NMS (18.882 $m^2\ g^{-1}$; 0.036 $cm^3\ g^{-1}$). This observation suggests that the deliberate design of the NMS nanosheets covering BP surface method leads to an enhanced specific surface area and pore volume, which ultimately facilitates the storage of electrolyte ions and charges. The pore-size distribution of the BJH analysis reveals mean pore diameter of 13 nm, as shown in Figure S3, Supporting Information. This concentration indicates the presence of a mesoporous structure in the NMS/BP material, which is known to enhance the diffusion of ions at a rapid pace. The comparative electrochemical performance of several Ni/Mo-based negative electrode materials is shown in **Table 1**.[38,69–75]

2.3. Electrochemical Performance of $NiMo_3S_4$ and $NiMo_3S_4$/BP

A three-electrode setup on the CC Ni-foam substrate was implemented to evaluate the electrochemical features of the individual active electrode. The working electrode was directly used, the counter electrode used Pt foil, and the Ag/AgCl was employed as a reference electrode. **Figure 5a** shows a comparative electrochemical performance of pristine NMS, and NMS/BP was tested in 0.5 M K_2SO_4, wherein the CV curves were recorded at 40 mV s^{-1}. The reversible redox characteristics of $Ni^{2+}/Ni^{3+}/Mo^{2+}/Mo^{6+}$ resulted in a pair of Faradaic redox peaks throughout the potential range of −0.2 to −1 V for pristine NMS electrode, whereas the NMS/BP electrode showed the enhanced potential window of −1 to 0 V, along with the improved current response. Redox peaks were attributed to interactions between electrodes and electrolytes, with postulated processes as follows:[18,48–50]

$$NiMo_3S_4 + xK^+ + xe^- \leftrightarrow K_x - NiMo_3S_4 \quad (6)$$

Figure 5d illustrates that the recorded CV curves resemble quasi-rectangular forms. As the sweep rate increases from 5

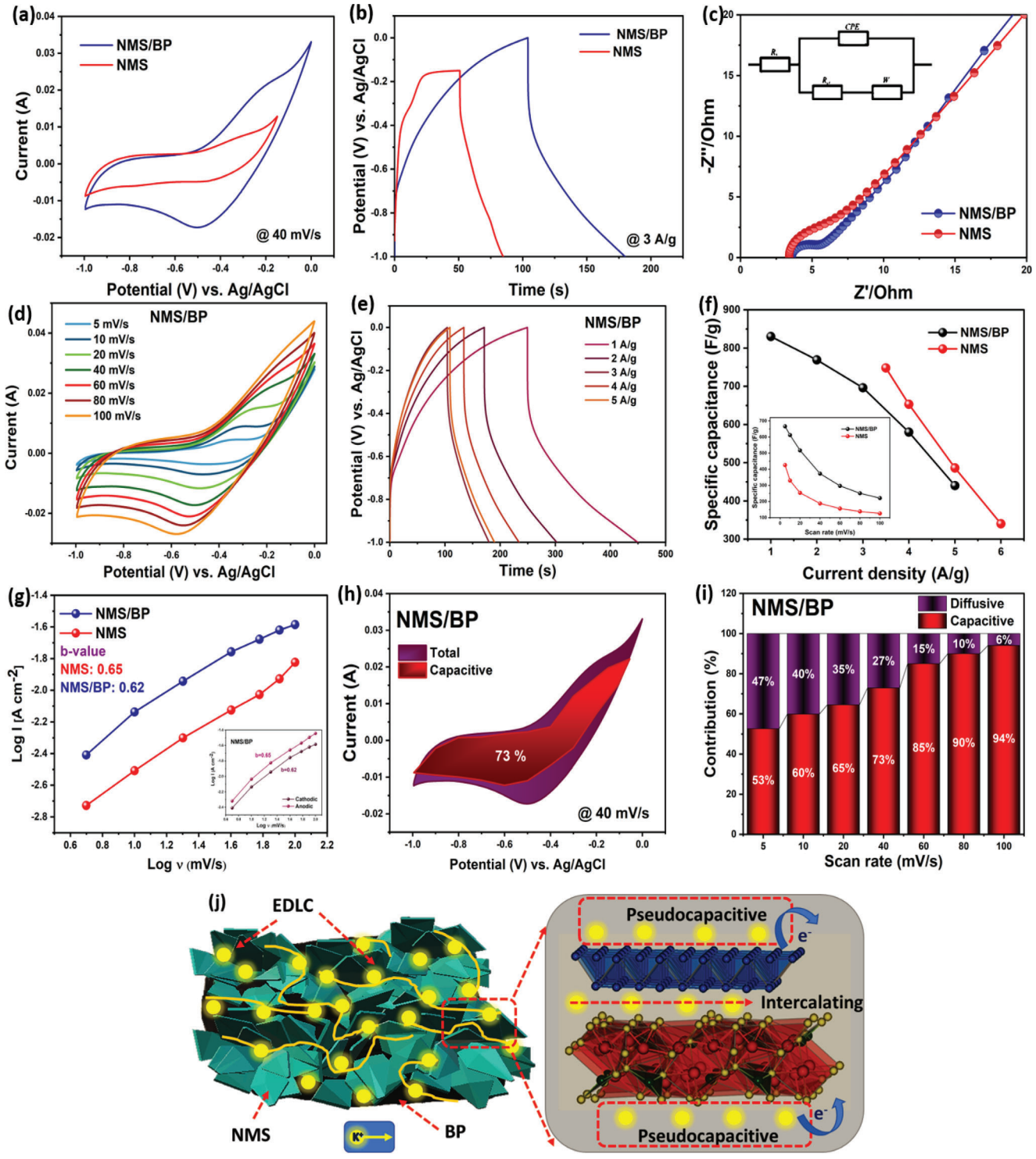

Figure 5. Comparative electrochemical performance in 0.5 M K_2SO_4: a) CV curves at 40 mV s^{-1}. b) GCD curves at 3 A g^{-1}. c) Nyquist plot (inset-equivalent circuit). d) CV curves of NMS/BP. e) GCD profiles of NMS/BP. f) Specific capacitance versus current density, g) linear relation between peak current and scan rates, h,i) charge–storage kinetics of NMS/BP, j) schematic of structural benefit and charge-transfer process during the electrochemical performance of NMS/BP electrode.

Table 1. Comparative electrochemical performance of various Ni/Mo-based negative electrode materials.

Material	Electrolyte	Potential window [V]	Specific capacitance [F g^{-1}]	Testing condition	Ref.
p-MoS_2/BP	0.5 M Na_2SO_4	−1 to 0	144	1 A g^{-1}	[38]
GQD-MoS_2/NSG-20	6 M KOH	−1.2 to 0	564.3	10 mV s^{-1}	[69]
CNF-MoS_2	3 M KOH	−0.9 to 0	138.9	0.5 A g^{-1}	[70]
KF@MoS_2@rGO	0.5 M Na_2SO_4	−1 to −0.4	347	0.5 A g^{-1}	[71]
Ni_xS_y@CoS	6 M KOH	−0.1 to 0.25	2291	1 A g^{-1}	[72]
Ni_9S_8@MoS_2	1 M KOH	−0.3 to 0.6	907	2 A g^{-1}	[73]
PPY@$MnMoO_4$	2 M KCl	−0.6 to 0.4	313	0.2 A g^{-1}	[74]
Mn–MoO_4/GO	1 M Na_2SO_4	−0.8 to 0.8	302.8	0.1 A g^{-1}	[75]
$NiMo_3S_4$/BP	0.5 M K_2SO_4	−1 to 0	840	1 A g^{-1}	Present work

to 100 mV s^{-1}, the CV curves remain consistent, proving that the NMS/BP hybrid electrode influences rapid charge-transfer dynamics.[46] All electrode CV curves exhibit similar traces, without any significant discrepancies even at higher scan rates. The specific capacitance calculated from CV curves potentially determines the faradic and capacitive contributions. The slight shift in anodic and cathodic peaks toward positive and negative potentials with increasing scan rates explains the kinetic reversibility in the redox processes carried on by ohmic resistance and polarization. Figure 5b demonstrates the comparative GCD curves at 3 A g^{-1} with the same potential as CV analysis; the NMS and NMS/BP electrode GCD curves show non-linear time variability with respect to the potential. The NMS/BP hybrid electrode GCD curves at different current densities are shown in Figure 5e. It shows co-existence of pseudocapacitive and EDLC behaviors, confirming hybrid capacitance nature which is in well agreement with the CV curves. Figure 5f gives the specific capacitance values at various current densities wherein the NMS/BP hybrid shows excellent specific capacitance of 840, 769, 697, 561, and 440 F g^{-1} at 1, 2, 3, 4, and 5 A g^{-1} of current densities, respectively. The pristine NMS shows high specific capacitance of 748 F g^{-1} at 3.5 A g^{-1}. The CV and GCD analyses of pristine NMS are displayed in Figures S4a,S4b, Supporting Information, respectively. To further understand the charge storage mechanism of our hybrid material electrodes, we interconnect scan rate (ν) and oxidation peak current (i) from cyclic voltammograms to determine capacitance from surface redox reaction $i \propto \nu$ or quasi bulk intercalation $i \propto \sqrt{\nu}$. Figure 5g exhibits the diffusion-controlled process correctly dominates capacitance for the NMS/BP electrode, as evidenced by the linear plot between peak current (i) and scan rate square root of $\sqrt{\nu}$. The power law equation gives a peak current "i_p" at various scan rates "ν" from the CV curves,[48] which are employed to investigate the kinetics of the charge storage mechanism of the fabricated electrodes, which is given as:

$$i_p = i_s + i_d = ab^{\nu} \tag{7}$$

In general, the capacitive controlled kinetics represents $b = 1$, whereas diffusive controlled represents $b = 0.5$. The slope of the uninterrupted continuous line between log i_p and log v in Figure 5g indicates the prepared electrodes' b values. NMS/BP and NMS electrodes had hybrid b values of 0.62 and 0.65, indicating a hybrid nature with capacitive regulated nature through dominating surface-controlled kinetics over diffusion-controlled processes, resulting in the quick electrochemical reaction process. A modified power-law equation was used to determine the diffusive and capacitive contributions of the NMS/BP electrode, using the current response with applied voltage at a given scan rate.[23,55]

$$i(V) = K_1 \upsilon + K_2 \upsilon^{1/2} \tag{8}$$

$$i(V) / \upsilon^{1/2} = K_1 \upsilon^{1/2} + K_2 \tag{9}$$

where K_1 and K_2 represent capacitive and diffusion-controlled processes, respectively. Figure 5h demonstrates 73% capacitive and 27% diffusive regulated contribution at a sweep rate of 40 mV s^{-1} for NMS/BP electrode. As illustrated in Figure 5i, the capacitive component stores most of the charge at higher scan rates due to the shortened ion-diffusion route. Capacitive charge storage accounts for 53% for NMS/BP electrode at 5 mV s^{-1} of scan rate. An NMS nanosheets structure on BP nanosheets lowers ion diffusion distance, resulting in a diffusion-controlled ion intercalation mechanism that adds to the diffusion contribution NMS/BP hybrid structure. To investigate further about ion diffusion, charge-transfer kinetics, and conductivity, electrochemical impedance spectroscopy (EIS) is performed. Figure 5c shows constructed electrode Nyquist plots. High-frequency semi-circle traces yield the charge-transfer resistance, R_{ct}. More capacitive characteristics are shown by the vertically increased straight trace. R_{ct} values for NMS/BP and NMS are 1.95 and 3.51 Ω, respectively. The broad surface area of BP nanosheets and the cross-bridge effect from edge sites of NMS explains hybrid electrodes low R_{ct} values and high conductivity. The NMS/BP electrode offers the following benefits, as indicated in Figure 5j. NMS/BP hybrid system improvements impact the supercapacitor electrode by showing improvement due to synergistic effects, including increased active sites from BP, which enhances interfacial reaction, ion transport channel, and electrical conductivity.

2.4. Theoretical Analysis of $NiMo_3S_4$/BP

2.4.1. Structural Properties

Figure 6a,b displays the side and top view of the optimized structure of bulk $NiMo_3S_4$. DFT optimized lattice parameters are $a = 6.384$Å, $b = c = 6.533$Å, $\alpha = \beta = 97.770°$, and $\gamma = 91.287°$.

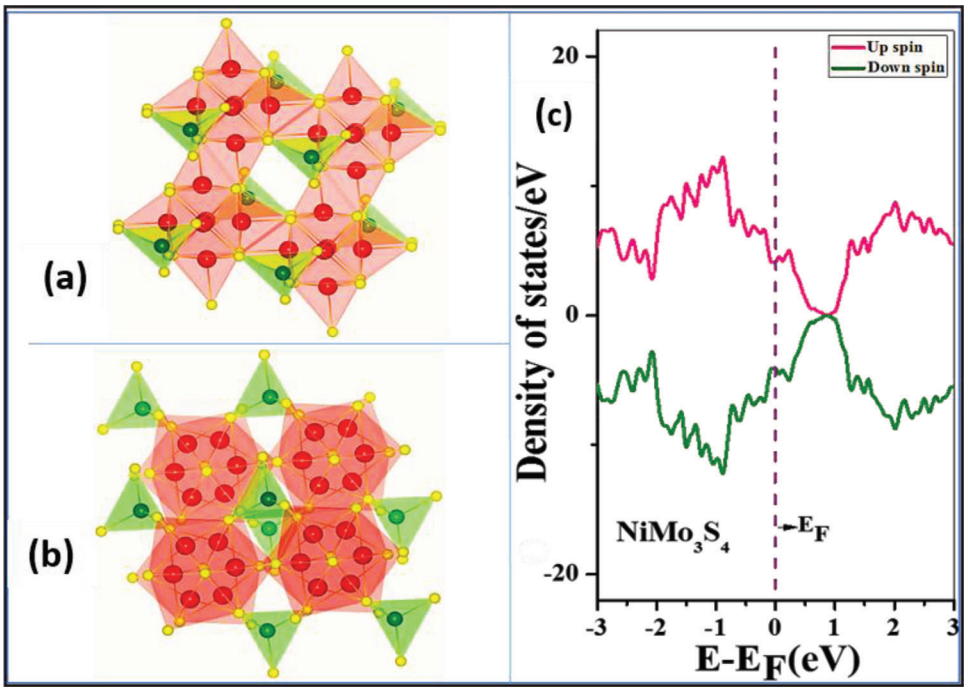

Figure 6. DFT optimized bulk $NiMo_3S_4$ structure with a) side view, b) top view, and c) total density of states (TDOS) plot; Yellow, Red, and Green are S, Mo, and Ni atoms respectively.

The total density of states plot provided in Figure 6c exhibits finite electronic states at the Fermi level, indicating the zero-band gap and metallic nature of the bulk $NiMo_3S_4$. While generating the hybrid layers NMS/BP, initially we take (040) plane of BP and (111) plane of NMS. The reason for selection of these specific planes is that they represent one of the highest intensity peaks among various peaks in their respective XRDs. The top view of the optimized (111) plane of NMS is depicted in **Figure** 7a. Once these planes are optimized, we make the hybrid structure by combining the two layers with interplanar separation of ≈3.5 Å. The

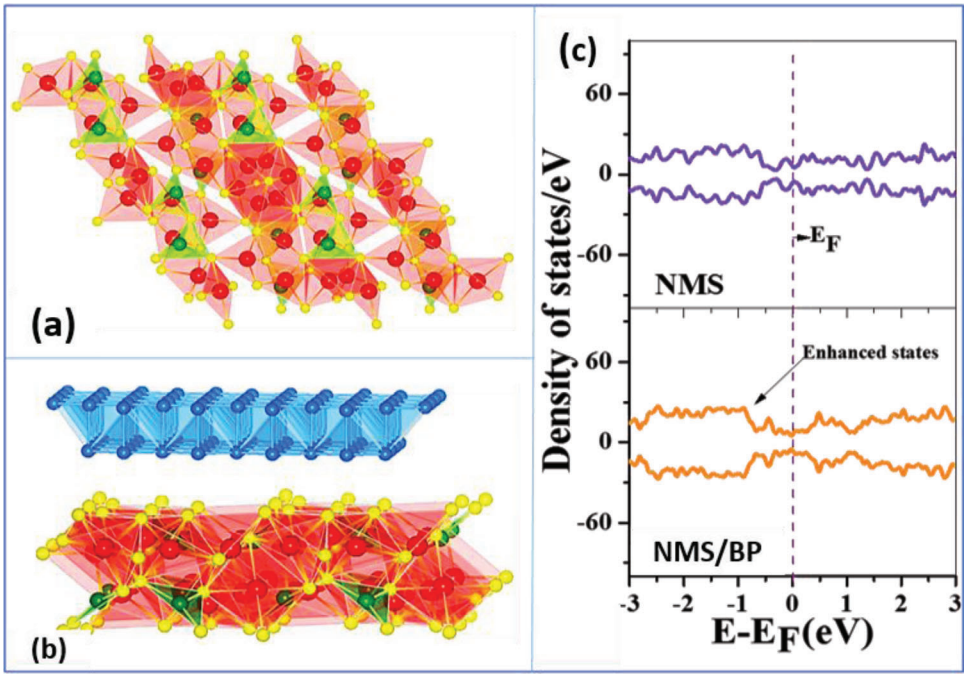

Figure 7. a) 2 × 2 supercell of (111) NMS. b) NMS/BP hybrid structure and c) total density of states (TDOS) plot for NMS and NMS/BP; Yellow, Blue, Green, and Red are S, P, Ni, and Mo atoms, respectively.

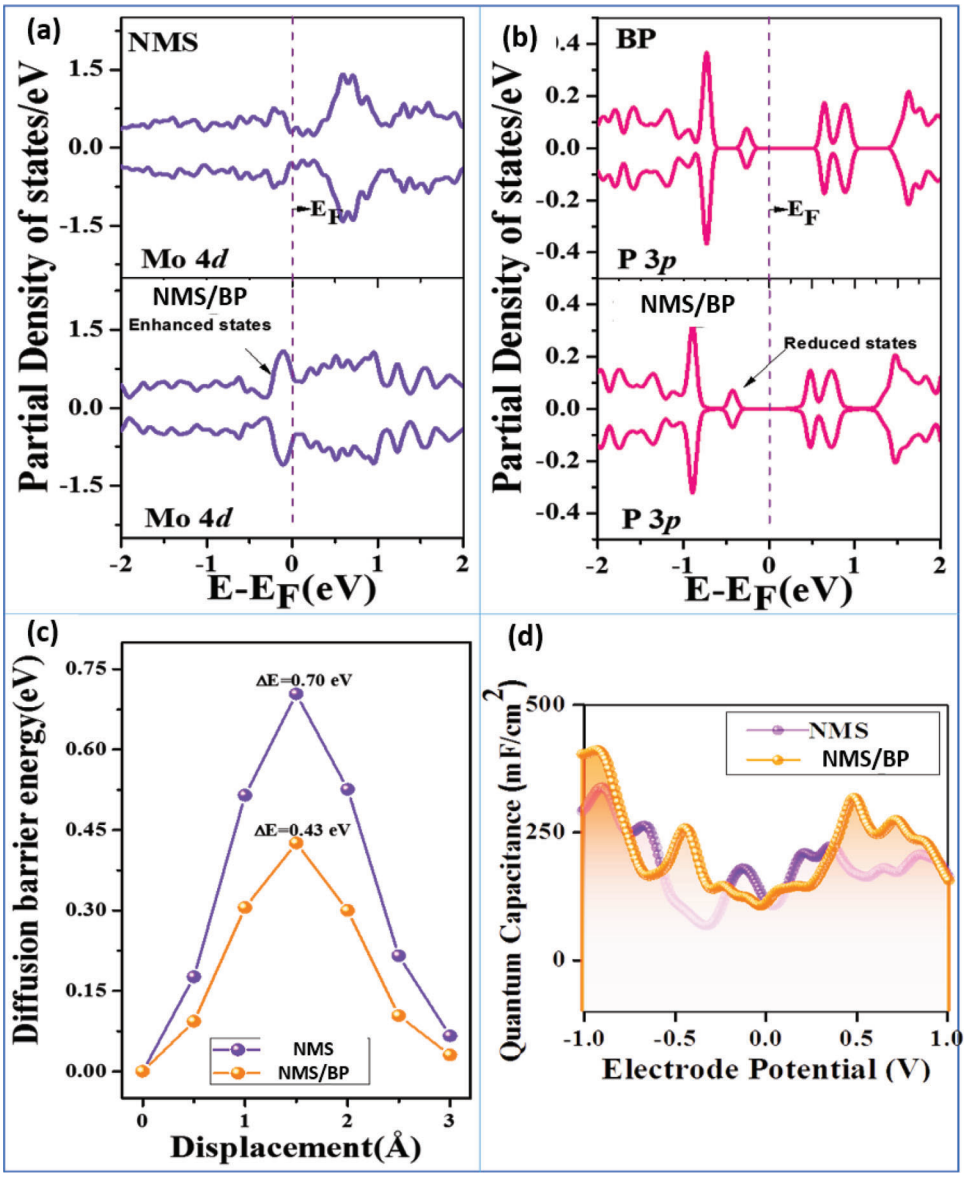

Figure 8. a) PDOS plot for Mo 4d orbital of NMS before and after hybridization with BP, b) PDOS plot for P 3p orbital of BP before and after hybridization with NMS, and c) diffusion energy barrier plot for K+ ions in NMS and NMS/BP. d) Quantum capacitance plot with the electrode potential for NMS and NMS/BP.

optimized hybrid NMS/BP structure is as shown in Figure 7b. Here, we maintain a sufficient vacuum of 20 Å along the *z* direction to avoid any further layer-to-layer interaction in the perpendicular direction. The supercell selected for hybrid has a dimension of 2 × 2 × 1 times the unit cell to involve enough number of atomic interactions in the plane.

2.4.2. Electronic and Orbital Interactions

In Figure 7c, we present the TDOS plot for NMS (111) plane (upper panel) along with its hybrid NMS/BP (lower panel). In these two plots, we can observe that there is an enhancement in electronic states near Fermi level due to the addition of BP to NMS. This evidence that the conductivity of hybrid structure shows improvement thus proves to be better energy storage material than single layer of NMS.

To get insights of orbital interactions, we plot the partial density of states (PDOS) of Mo 4d and P 3p orbital of NMS and BP before and after hybridization, as provided in **Figure 8a,b**. For Mo 4d orbital, there is a net charge gain after hybridization with BP, which can be seen from enhancement of states near fermi level for the hybrid structure compared to NMS (Figure 8a). Further, P 3p orbital of BP shows loss of states after hybridization with NMS, as depicted in Figure 8b. To support these qualitative PDOS plots in terms of quantitative charge transfer, we further do the Bader charge partitioning.[59] It is worth mentioning that the Bader charge partitioning is a more realistic quantitative

aspect; whereas, the PDOS is just qualitative in nature. From Bader charge partitioning, we find that there is a small charge transfer of the order of 0.02e from BP to NMS even though this much charge transfer has played a significant role in overall improvement of conductivity of hybrid as seen from DOS plots. As seen from Figure 8c, the lower diffusion energy barrier for the electrolyte K^+ ions in the hybrid structure is attributed to improved charge transfer performance for the hybrid NMS/BP as observed in the experiment.

2.4.3. Computation of Quantum Capacitance

Density functional theory was also applied to understand quantum capacitance variation of NMS and its hybrid counterpart NMS/BP. For this calculation, we have estimated the quantum capacitance of NMS and NMS/BP with the help of earlier well-established relation.[60–62]

$$C_Q = e^2 \int_{\infty}^{\infty} D(E)\, F_T\left(E - e\phi_G\right) dE \tag{10}$$

where D(E) is the total density of states and is the electrode potential of the system for which calculation is done. F_T(E) is the broadening function due to thermal effect given as;

$$F_T(E) = (4K_B T)^{-1} \sec h^2\left(E/2K_B T\right) \tag{11}$$

Figure 8d shows the variation of quantum capacitance vs electrode potential for NMS and hybrid NMS/BP. This plot clearly shows that there is an increase in quantum capacitance in the case of hybrid over the NMS. Thus, it gives the verification of the experimental readings for NMS and its hybrid. It may be observed that the increase in surface area and enhanced density of states due to BP layer addition may have affected the electrical conductivity, leading to higher charge storage capacity. Further, we can note that the quantum capacitance is substantial at nanoscale but, as far as experimental measurements are considered, it includes both quantum and electrical double layer capacitance.

2.5. Electrochemical Performance of Asymmetric Supercapacitor-$NiMo_3S_4$/BP // $NiCo_2S_4$@$Ti_3C_2T_x$ (NMS/BP//NCS/TCX)

In order to construct a functioning ASC device, the operating potential and optimal mass loading for both positive and negative electrodes were calculated by CV measurements at a constant scan rate of 20 mV s^{-1}. As $NiCo_2S_4/Ti_3C_2T_x$ and $NiMo_3S_4$/BP electrodes have potential ranges of 0.0 to +0.8 V (vs Ag/AgCl) (Figure S4c,d, Supporting Information) and −1 to 0.0 V (vs Ag/AgCl), respectively, the ASC device can display a potential window of 1.8 V. The charge balancing proposition (Q+ = Q−) determines the proper mass loading of negative to positive electrodes.[16] The ASC device was constructed using NCS/TCX as positive and NMS/BP as negative electrode and the performation performance optimization was carried out in a coin-cell assembly using aqueous 0.5 M K_2SO_4 electrolyte, respectively. **Figure** 9a shows NMS/BP//NCS/TCX asymmetric device operating voltage window optimization CV curves at 40 mV s^{-1}. Figure 9b shows the ASC device assembly with optimized positive and negative electrode mass ratios. The NMS/BP//NCS/TCX device had an enhanced capacitive area, upright current response, stable operating potential range of 1.8 V, and a sharp peak and sudden increase in current when the operational voltage was increased, indicating the parasitic oxygen evolution reaction caused by electrolytic decomposition.[16] Figure 9c represents the NMS/BP//NCS/TCX device traced quasi-rectangular CV curves at scan rates ranging from 5 to 100 mV s^{-1}, demonstrating its dominance over capacitive nature and excellent reversibility. Symmetric profiles from the GCD curves of NMS/BP//NCS/TCX device were determined at various current densities. As depicted in Figure 9d, a non-linear nature due to faradic processes was observed, which agreed with the CV plots and suggested excellent Coulombic efficiency and reversibility. The device displayed good energy storage performance, in terms of specific capacitance with 120 F g^{-1} at the minimum current density of 0.5 A g^{-1}. The NMS/BP//NCS/TCX asymmetric device exhibited specific capacitance of 109.3, 97.6, 86.2, 78.8, and 71.4 F g^{-1} for current densities of 0.6, 0.7, 0.8, 0.9, and 1 A g^{-1} respectively. In Figure 9e, the capacitance value increased with decreasing current density, considering charge storage was predominantly on the surface, and electrolytic ions could not completely intercalate between electrode layers. In addition, Coulombic efficiency acted as a function against current density. The lower current densities produced parasitic reactions that partly channeled the electrode, showing limited reversibility in electrochemical redox processes. Increasing current density eventually enhanced the Coulombic efficiency.

For practical applications, supercapacitor cycle stability is crucial. To evaluate NMS/BP//NCS/TCX device cycle stability, galvanostatic charge–discharge performance at 10 A g^{-1} is repeated. From Figure 9f, the results refer to the long-term life and stability of NMS/BP//NCS/TCX device asymmetric device by retaining the 86% of specific capacitance after 5000 GCD cycles. The device has outstanding reversibility as it exhibits 97% coulombic efficiency; the inset shows CV cycle after 5000 cycles and GCD curves at the 1st and 5000th cycle during stability. The inset shows FE-SEM image od NMS/BP electrode after stability test. The analysis demonstrates that the 3D hierarchical structure remains intact without significant morphological distortion. The vertical alignment of the NMS nanosheets on the BP support enhances electrical conductivity by augmenting the contact between the nanosheets and the substrate. The configuration of nanosheets in both electrodes allows for the exploitation of void between consecutive arrays of nanosheets (Figure S5, Supporting Information). This void is used as a reservoir for ions and regulates the amount of charge throughout each charging/discharging cycle. In this particular situation, the usage NMS nanosheets with distinct porosity frameworks facilitate the entry of ions; hence, enhancing the use of electroactive materials. The BP support exhibits superior characteristics such as rapid electron transport kinetics, minute internal resistance, and exceptional mechanical stability and flexibility. XRD analysis is performed to analyze the structural integrity of the electrode. Figure S6, Supporting Information illustrates that the K_2SO_4 electrolyte is responsible for the rise in intensity at ≈26° and 30°, which occurs after 5000 cycles of charge–discharge and coincides with the intercalation

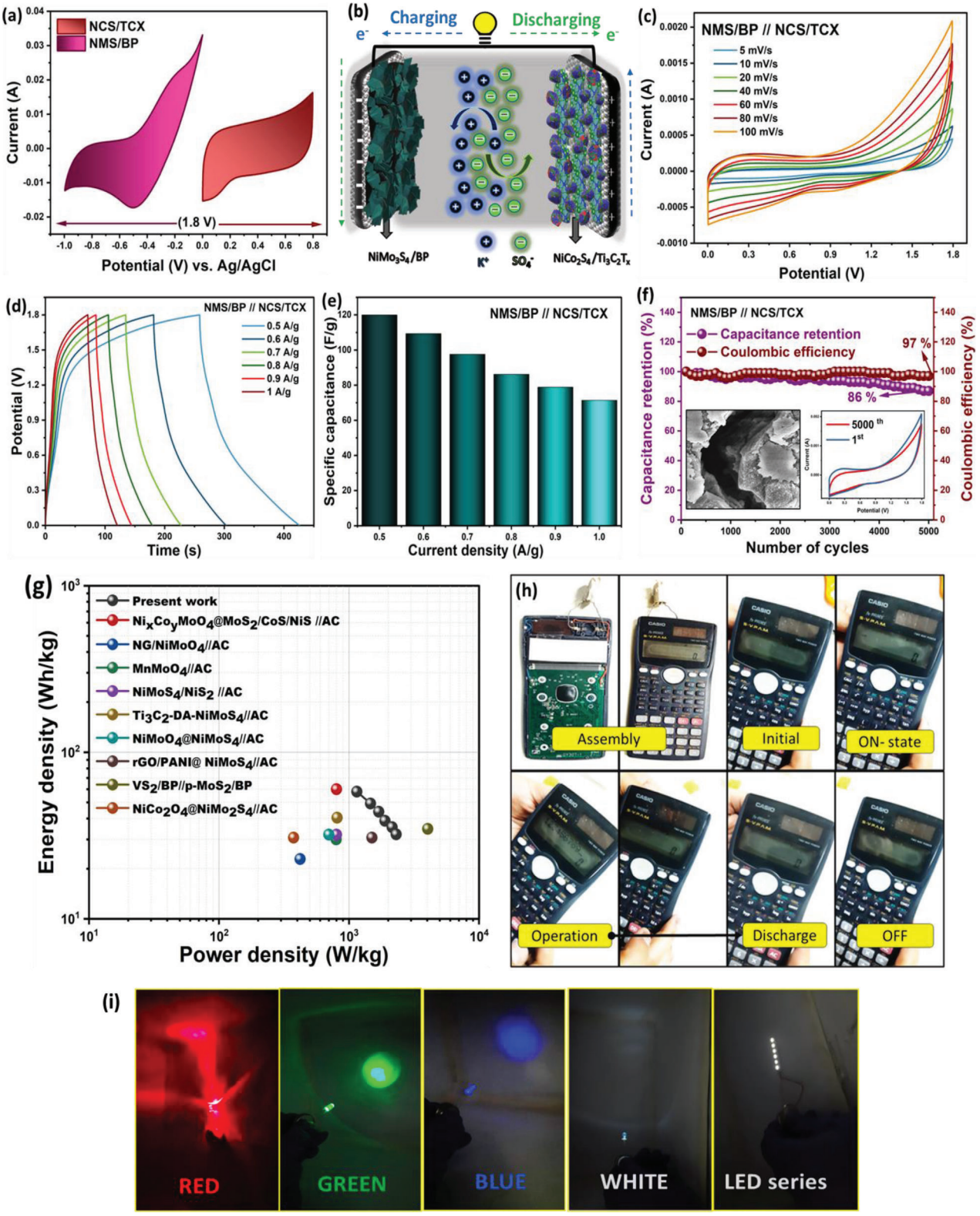

Figure 9. a) Comparative CV cycles of NMS/BP and its composite and NCS/TCX. b) Schematic of construction of NMS/BP//NCS/TCX ASC device. c) CV curves of ASC; d) GCD curves of ASC; e) specific capacitance (F/g) versus current density (A/g); f) cyclic stability (inset shows CV cycle after 5000 cycles and GCD curves at 1st and 5000th cycle during stability); g) comparative Ragone plot; h) example of employing the constructed ASC to illuminate an adaptable display with two ASC in series connections; and i) different colored LED illuminations, red, green, blue, yellow, white, and series of LED lights, with two ASC in series connections.

Table 2. Comparative electrochemical performance of Ni–Mo-based asymmetric devices.

Material	Specific capacitance [F g^{-1}]	Current density (A P^{-1})	Energy density [Wh kg^{-1}]	Power density [W kg^{-1}]	Cycling stability [% per cycles]	Ref.
$Ni_xCo_yMoO_4$@MoS_2/CoS/NiS // AC	173	1	60.7	800.40	94.4/5000	[63]
NG/$NiMoO_4$/ //AC	62.5	0.5	22.84	400	94.2/5000	[64]
$MnMoO_4$//AC	89	1	31.7	797	—	[65]
H-$NiMoS_4$/NiS_2// NCO	144.2	1	32	800	87.3/2000	[66]
rGO/PANI@$NiMoS_4$// AC	73.1	0.5	22.81	375	117.4/5000	[67]
VS_2/BP//p-MoS_2/BP	114	4	34.71	4031	90/5000	[38]
$NiCo_2O_4$@$NiMo_2S_4$// AC	98.4	0.5	30.73	374.9	84.2/10000	[68]
$NiCo_2S_4$/$Ti_3C_2T_x$ //$NiMo_3S_4$/BP	120	0.5	54	1148.53	86/5000	Present work

of K^+ ions into the NMS/BP hybrid. The slight shift in peaks at ≈27° in NMS structure and 41° toward lower degree (39.5°) indicates the expansion in interlayer spacing in BP, supported by the K_2SO_4 peak appearing in the XRD patterns, which indicates a persistent charge transportation of ions in K_2SO_4 electrolyte in the NMS/BP system. The XRD pattern shows that pseudocapacitive reactions remain stable throughout the process, preventing the formation of any extra phases during the electrochemical process dominated by diffusion process. The Ragone plot of asymmetric devices is shown in Figure 9g. The NMS/BP//NCS/TCX device offers an effective energy density of 54 Wh kg^{-1} and a power density of 1148.53 W kg^{-1}. Energy density appearing at 32.14 Wh kg^{-1} retains at 2305.12 W kg^{-1}, a noteworthy power density. The energy density and power density of the ASC surpass those of Ni/Mo- and 2D hybrids-based supercapacitor devices. **Table 2** provides the comparative electrochemical performance of Ni–Mo-based asymmetric devices. As revealed in Figure 9h, two NMS/BP//NCS/TCX ASC devices connected in series are capable of running a multi-function display for 30 s, demonstrating its practical application potential. As shown in Figure 9i, constructed NMS/BP//NCS/TCX device powers various coloured commercial LED lights by connecting two devices in series. The electrochemical energy storage capabilities of $NiMo_3S_4$/BP electrode are superior primarily because of practical advantages and ion transport pathways in the present experiment, which can be attributed to the following properties: i) The nucleation site from BP is essential for the formation of significant, desired shortcoming sites in $NiMo_3S_4$ nanostructures. These sites raise the lattice spacing, which promotes more stable energy storage performance. ii) NMS functions as spacer molecules in the NMS/BP hybrid, preventing BP from aggregating together and increasing surface area, electrical conductivity, and charge transfer resistance. The NMS/BP composite electrode material works in recital to enhance the electrochemical performance. iii) Large surface area, excellent electron transport, and high ion-diffusion rates are provided by the developed 3D hierarchical nano architectures with rich redox active sites of $NiMo_3S_4$ nanosheets, which are advantageous for the enhancement in the electrochemical performance. Last, iv) a robust mechanical scaffolding framework for $NiMo_3S_4$ nanosheets that inhibits aggregation during rapid charge/discharge cycles is provided by BP sheets. Further, the fabrication of a 3D BP structure is a very efficient method to further augment the characteristics of 2D BP materials. The advantages of a hierarchical 3D NMS nanostructure are as follows: the highly adjustable pore structure can enhance the specific surface area and facilitate the diffusion of ions, NMS network with excellent conductivity enables rapid electronic transfer, and the 3D connector structure can absorb volume variations during charge and discharge cycles. In addition, they offer an efficient electrically conductive pathway. Due to these benefits, $NiMo_3S_4$/BP 3D hierarchical nano architectures are synthesized, which greatly enhance electrochemical capabilities with outstanding specific capacity, rate capability, and cycle stability for an overall, asymmetric SC device.

3. Conclusion

In this work, a facile one-step in situ hydrothermal synthesis approach was employed for the construction of $NiMo_3S_4$/BP hybrid with a 3D hierarchical structure. In addition to supporting the BP and grafted by $NiMo_3S_4$, the hybrid offers extra support that enhances redox active sites for electrochemical reaction, which helps many ion transfer channels avoid self-stacking. $NiMo_3S_4$/BP hybrid, after optimization, displays a high specific capacity of 830 F g^{-1} at 1 A g^{-1} compared to pristine $NiMo_3S_4$ electrode. The fabricated $NiMo_3S_4$/BP//$NiCo_2S_4$/$Ti_3C_2T_x$ asymmetric supercapacitor exhibits better specific capacitance of 120 F g^{-1} at 0.5 A g^{-1}, with a high energy density of 54 Wh kg^{-1} at 1148.53 W kg^{-1}, good cycle stability, and capacity retention of 86% and 97% of coulombic efficiency after 5000 cycles. The potential use of the fabricated supercapacitor devices based on $NiMo_3S_4$/BP hybrid is demonstrated with a satisfactory performance. The experimental findings are supported by theoretical analysis using DFT studies. The structural and electronic properties of NMS/BP show enhancement in electronic states near the Fermi level for the hybrid structure. This enhancement in electronic states may be responsible for the increase in conductivity as well as an increase in quantum capacitance, leading to superior charge storage performance for the hybrid structure.

4. Experimental Section

Materials: For the synthesis of $NiMo_3S_4$ and $NiMo_3S_4$/BP, a simple hydrothermal technique was used. Without any extra modifications, all of the analytical-grade compounds were utilized. Ammonium molybdate tetrahydrate ($(NH_4)_6Mo_7O_{24}.4H_2O$, SDFCL), nickel nitrate hexahydrate ($Ni(NO_3)_2.6H_2O$, SDFCL), thioacetamide (C_2H_5NS, SRL), red phosphorus (RP, ISOCHEM), ethylene diamine ($C_2H_4(NH_2)_2$, AVRA), K_2SO_4,

ethanol LR (SDFCL), Nafion solution (5 wt% in mixture of lower aliphatic alcohols and 45% water), acetone LR, hydrochloric acid (HCl), Ni-foam, and distilled water.

Synthesis of BP: The process of synthesizing BP from RP is shown in Figure 1a. It involves a standard bottom–up solvothermal reaction in ethylene diamine (ED). Prior to solvothermal treatment, RP was refluxed at 70 °C for 12 h in an oil bath; while, being continuously stirred and pre-treated with DI water (5 wt%). After being cleaned with distilled water, the final product was dried at 60 °C in a vacuum oven. Following being pre-treated, the RP powder was mixed with 12.8 wt% of ED and stirred magnetically. Afterward, the homogenized solution was put in a 50 mL autoclave lined with Teflon and subjected to solvothermal treatment for 24 h at 200 °C in a hot-air oven. After eliminating impurities with ethanol and DI water, the final product was dried in a vacuum oven at 60 °C overnight.

Synthesis of $NiMo_3S_4$/BP Hybrid: For the construction of $NiMo_3S_4$ and $NiMo_3S_4$/BP hybrid, typically, 3 mM of $Ni(NO_3)_2.6H_2O$ and 9 mM of $(NH_4)_6Mo_7O_{24}.4H_2O$ were dispersed in 30 mL of distilled water; then, 12 mM of thioacetamide (C_2H_5NS) was gradually added. The mixture was then magnetically stirred for 45 min at room temperature until a homogenous solution was formed. The mixture was subsequently transferred to a 50 mL stainless-steel autoclave with a Teflon lining. The hydrothermal treatment was carried out for 12 h at 200 °C. $NiMo_3S_4$/BP hybrid formation was carried out by adding 30 mg of produced BP powder to the precursors and treating them hydrothermally at 200 °C for a duration of 12 h. The final product was filtrated and then cleaned with ethanol and distilled water. The last step involved vacuum drying the product at 60 °C for 12 h and annealing it in an Ar environment for 3 h at 350 °C. The stepwise synthesis procedure is illustrated in Figure 1b.

Material Characterization: By employing X-ray diffraction (XRD, Rigaku Ultima IV with NI-filter for Cu-Kα radiation, $\lambda = 0.1541$ nm), the phase purity and crystallographic details of the produced materials were examined. Field emission scanning electron microscopy (FESEM, JEOL JSM-7100F, JEOL Ltd., Singapore) was used to perform the elemental and morphological investigations. X-ray photoelectron spectroscopy (XPS, Thermo K Alpha+ spectrometer, Al Kα X-rays with 1486.6 eV energy) was employed for the compositional study under ultrahigh vacuum conditions. Further, extensive morphological and structural analyses were undertaken through transmission electron microscopy (TEM, TALOS F200S G2, 200 kV, FEG, CMOS camera 4k 4k).

Electrochemical Characterization: The electrochemical performance of as-prepared materials was assessed in 0.5 M K_2SO_4. The redox process was investigated using a three-electrode set-up, with Pt wire as the counter and Ag/AgCl as the reference electrodes. Electrodes were fabricated on cleaned Ni foam using a drop cast process (0.78 cm^2 area, 1 M HCl treatment, distilled water, and acetone LR). 1 mg of material was combined in a 1:19 Nafion and ethanol solution and sonicate for 5–10 min. A slurry was dropped over Ni-foam and vacuum-dried at 60 °C. These electrodes were used as working electrodes after being pellet-crushed using a hydraulic press at 5 tonnes of pressure. Electrochemical characterizations of constructed electrodes, comprising CV, GCD, and EIS, had been carried out using a CorrTest CS350 workstation in Wuhan, China. All electrodes had been investigated with EIS at open circuit potential using a frequency range of 0.01 Hz to 100 kHz and a sinusoidal potential of 5 mV. The stability test was determined using GCD profiles and gravimetric capacitance values.

Fabrication of Asymmetric Supercapacitors: The asymmetric supercapacitor was constructed by implementing a conventional coin cell packing (CR2032). A Whatman filter paper (Whatman qualitative filter paper with a diameter of 125 mm / thickness of 200 µm) separated the $NiMo_3S_4$/BP electrode as the negative with an active mass of 2.6 mg and the previously reported $NiCo_2S_4/Ti_3C_2T_x$ as the positive electrode with an active mass of 5 mg.[16] An aqueous solution of 0.5 M K_2SO_4 electrolyte was loaded onto the working electrodes and sealed in the coin cell using a crimper.

The mass of each electrode was determined by applying the mass balance equation, employing the charge balance Q+ = Q−.

$$\frac{m_+}{m_-} = \frac{C_- \times \Delta V_-}{C_+ \times \Delta V_+} \tag{12}$$

Asymmetric supercapacitors could be optimized by adjusting the average mass relation between the electrodes, m+/m−.[16]

The specific capacitance calculated from cyclic voltammetry,

$$Csp = \frac{\int I(V)\,dv}{[m\,s\Delta V]} \tag{13}$$

$I(V)$dV is the CV curve area, m is the electrode material mass, s is the scan rate, and V is the potential window.

Specific capacitance from the galvanostatic charge–discharge cycle,

$$Csp = \frac{I\Delta t}{m\Delta V} \tag{14}$$

Here, I is current, m is electrode mass, t is discharging time, and V is a potential window. The current/mass and discharge time/potential window could be calculated using the slope of the discharging curve utilizing galvanostatic charge–discharge profiles ($\Delta t/\Delta V$).

The energy density of an ASC device was calculated using the following formula,

$$Ed = 0.5xCspx(\Delta V)^2 \tag{15}$$

where, ΔV is the potential window and Csp is a specific capacitance calculated from GCD plots.

The power density of an ASC device was calculated by using the following formula:

$$Pd = \frac{Ed \times 3600}{\Delta t} \tag{16}$$

where Δt is the discharging time and Ed refers to energy density.

Computational Details: To perform the density functional theory (DFT) calculations, the VIENNA ab initio simulation package (VASP) code[51,52] had been used. The projector-augmented wave (PAW)[53] functional for pseudopotentials was selected for the present system. Further to undertake the ion–ion and ion–electron interactions, the GGA[54,55] exchange-correlational functional was applied. The Hellmann–Feynman forces and energy were converged till the accuracy of 0.01 eV $Å^{-1}$ and 10–5 eV, respectively were reached. The plane wave cutoff was taken as 520 eV. For Brillouin zone sampling, a Monkhorst scheme[56] with grid points 5 × 5 × 1 and 7 × 7 × 1 was chosen for optimization and electronic calculations, respectively. In the case of bulk optimization, theBrillouin zone was resampled to Monkhorst grid points 5 × 5 × 5. Sufficient vacuum had been introduced to avoid layer-to-layer interaction between the layers of hybrid structure. For diffusion energy barrier calculation of K+ ions, the climbing image nudged elastic band (CI-NEB) method was used.[57,58] In this, a total of seven images including the initial and final relaxations were used for the NEB configuration.

Supporting Information

Supporting Information is available from the Wiley Online Library or from the author.

Acknowledgements

The authors gratefully acknowledge financial assistance from the SERB Core Research Grant (Grant No. CRG/2022/000897), the Department of Science and Technology (DST/NM/NT/2019/205(G)), and the Minor Research Project Grant, Jain University (JU/MRP/CNMS/29/2023). CSR acknowledges the National Research Foundation of Korea for the Brain Pool program funded by the Ministry of Science and ICT, South Korea (Grant No. RS-2023-00222186). This work was supported by the National Research Foundation of Korea (NRF) and the Commercialization Promotion Agency for R&D Outcomes (COMPA) funded by the Ministry of Science and ICT (Grant No.: RS-2023-00217581, RS-2023-00304768).

Conflict of Interest

The authors declare no conflict of interest.

Data Availability Statement

The data that support the findings of this study are available from the corresponding author upon reasonable request.

Keywords

asymmetric supercapacitor, black phosphorous, density functional theory (DFT), hybrid nanostructure, $NiMo_3S_4$

Received: November 6, 2023
Revised: January 9, 2024
Published online:

[1] A. Riaz, M. R. Sarker, M. H. Saad, R. Mohamed, *Sensors* **2021**, *21*, 5041.
[2] S. M. Benoy, M. Pandey, D. Bhattacharjya, B. K. Saikia, *J. Energy Storage* **2022**, *52*, 104938.
[3] S. Y. Attia, S. G. Mohamed, Y. F. Barakat, H. H. Hassan, W. A. l Zoubi, *Rev. Inorg. Chem.* **2022**, *42*, 53.
[4] S. Huang, X. Zhu, S. Sarkar, Y. Zhao, *APL Mater.* **2019**, *7*, 100901.
[5] Y. Shao, M. F. El-Kady, J. Sun, Y. Li, Q. Zhang, M. Zhu, H. Wang, B. Dunn, R. B. Kaner, *Chem. Rev.* **2018**, *118*, 9233.
[6] V. Molahalli, K. Bijapur, G. Soman, G. Hegde, *Crit. Rev. Solid State Mater. Sci.* **2023**, 1.
[7] N. Flores-Diaz, F. De Rossi, A. Das, M. Deepa, F. Brunetti, M. Freitag, *Chem. Rev.* **2023**, *123*, 9327.
[8] B. Arumugam, G. Mayakrishnan, S. K. Subburayan Manickavasagam, S. C. Kim, R. Vanaraj, *Crystals* **2023**, *13*, 1118.
[9] B. Raj, A. K. Padhy, S. Basu, M. Mohapatra, *J. Electrochem. Soc.* **2020**, *167*, 136501.
[10] a) M. Pathak, S. M. Jeong, C. S. Rout, *J. Energy Storage* **2023**, *73*, 108881. b) A. Vedpathak, T. Shinde, M. A. Desai, B. R. Thombare, R. Humane, S. A. Raut, R. Kalubarme, S. D. Sartale, S. Bhagwat, *ACS Appl. Energy Mater.* **2023**, *6*, 4693.
[11] M. R. Pallavolu, S. Vallem, R. R. Nallapureddy, S. Adem, S. W. Joo, *ACS Appl. Energy Mater.* **2023**, *6*, 812.
[12] M. Pathak, S. R. Polaki, C. S. Rout, *RSC Adv.* **2022**, *12*, 10788.
[13] X. Y. Yu, X. W. (David) Lou, *Adv. Energy Mater.* **2018**, *8*, 1701592.
[14] M. Pathak, C. S. Rout, *Adv. Compos. Hybrid Mater.* **2022**, *5*, 1404.
[15] T. Chen, S. Wei, Z. Wang, *ChemPlusChem* **2020**, *85*, 43.
[16] D. Kong, Y. Wang, Y. V. Lim, S. Huang, J. Zhang, B. Liu, T. Chen, H. Y. Yang, *Nano Energy* **2018**, *49*, 460.
[17] Y. Li, P. Kamdem, X.-J. Jin, *Dalton Trans.* **2020**, *49*, 7807.
[18] M. Pathak, C. S. Rout, *J. Electron. Mater.* **2023**, *52*, 1668.
[19] R. Manikandan, C. J. Raj, G. Nagaraju, M. Pyo, B. C. Kim, *J. Mater. Chem. A* **2019**, *7*, 25467.
[20] S. Ghosh, P. Samanta, W. Jang, C.-M. Yang, N. C. Murmu, T. Kuila, *ACS Appl. Energy Mater.* **2022**, *5*, 1528.
[21] S. Anand, A. Choudhury, *Mater. Chem. Phys.* **2023**, *299*, 127517.
[22] K. Namsheer, S. Thomas, A. Sharma, S. A. Thomas, K. A. Sree Raj, V. Kumar, A. Gagliardi, A. Aravind, C. S. Rout, *Nanotechnology* **2022**, *33*, 445703.
[23] M. Pathak, D. Tamang, M. Kandasamy, B. Chakraborty, C. S. Rout, *Appl. Mater. Today* **2020**, *19*, 100568.
[24] R. Sankar Ganesh, K. Silambarasan, E. Durgadevi, M. Navaneethan, S. Ponnusamy, C. Y. Kong, C. Muthamizhchelvan, Y. Shimura, Y. Hayakawa, *Appl. Surf. Sci.* **2019**, *480*, 177.
[25] D. Kong, C. Cheng, Y. Wang, J. I. Wong, Y. Yang, H. Y. Yang, *J. Mater. Chem. A* **2015**, *3*, 16150.
[26] L. Shao, X. Qian, X. Wang, H. Li, R. Yan, L. Hou, *Electrochim. Acta* **2016**, *213*, 236.
[27] S. Chandrasekaran, T. Ma, Z. Hu, Q. Liu, C. Zhan, Y. Li, C. Bowen, H. Lu, Y. Liu, *Appl. Catal., B* **2023**, *338*, 123007.
[28] T. Wu, Z. Xu, X. Wang, M. Luo, Y. Xia, X. Zhang, J. Li, J. Liu, J. Wang, H.-L. Wang, F. Huang, *Appl. Catal., B* **2023**, *323*, 122126.
[29] Y. Chen, Z. Lai, X. Zhang, Z. Fan, Q. He, C. Tan, H. Zhang, *Nat. Rev. Chem.* **2020**, *4*, 243.
[30] S. Li, M. Xie, X. Zhang, N. Wang, R. Wang, Y. Xu, H. Lin, Y. Jiao, J. Chen, *Chem. Eng. J.* **2023**, *475*, 146172.
[31] S. Li, H. Chai, L. Zhang, Y. Xu, Y. Jiao, J. Chen, *J. Colloid Interface Sci.* **2023**, *642*, 235.
[32] S. Sarkar, P. Howli, B. Das, N. S. Das, M. Samanta, G. C. Das, K. K. Chattopadhyay, *ACS Appl. Mater. Interfaces* **2017**, *9*, 22652.
[33] K. A. Sree Raj, A. S. Shajahan, B. Chakraborty, C. S. Rout, *Chemistry* **2020**, *26*, 6662.
[34] Y. Zhou, M. Zhang, Z. Guo, L. Miao, S.-T. Han, Z. Wang, X. Zhang, H. Zhang, Z. Peng, *Mater. Horiz.* **2017**, *4*, 997.
[35] Y. Zhao, Y. Chen, Y.-H. Zhang, S.-F. Liu, *Mater. Chem. Phys.* **2017**, *189*, 215.
[36] J. He, D. He, Y. Wang, Q. Cui, M. Z. Bellus, H.-Y. Chiu, H. Zhao, *ACS Nano* **2015**, *9*, 6436.
[37] T. Liang, Y. Liu, Y. Cheng, F. Ma, Z. Dai, *ChemCatChem* **2020**, *12*, 2840.
[38] S. Radhakrishnan, N. Kuniyil, A. Sharma, C. S. Rout, *Energy Fuels* **2023**, *37*, 3196.
[39] S. Radhakrishnan, S. R. K. A., S. R. Kumar, P. Johari, C. S. Rout, *Nanotechnology* **2021**, *32*, 155403.
[40] N. K., C. S. Rout, *J. Mater. Chem. A* **2021**, *9*, 8248.
[41] R. Murugan, A. Rebekah, D. Navadeepthy, C. Viswanathan, N. Ponpandian, *Int. J. Hydrogen Energy* **2023**, *48*, 36389.
[42] Y. Wang, M. He, S. Ma, C. Yang, M. Yu, G. Yin, P. Zuo, *J. Phys. Chem. Lett.* **2020**, *11*, 2708.
[43] a) O. Bars, J. Guillevic, D. Grandjean, *J. Solid State Chem.* **1973**, *6*, 335. b) Materials Data on NiMo3S4 by Materials Project, (accessed: December 2023), https://doi.org/10.17188/1284254.
[44] J. M. van den Berg, *Inorg. Chim. Acta* **1968**, *2*, 216.
[45] H. Fukuoka, K. Masuoka, T. Hanaoka, K. Inumaru, *Inorg. Chem.* **2013**, *52*, 7918.
[46] J. Balamurugan, C. Li, V. Aravindan, N. H. Kim, J. H. Lee, *Adv. Funct. Mater.* **2018**, *28*, 1803287.
[47] F. Liao, J. Światowska, V. Maurice, A. Seyeux, L. H. Klein, S. Zanna, P. Marcus, *Appl. Surf. Sci.* **2013**, *283*, 888.
[48] B. Kirubasankar, M. Narayanasamy, J. Yang, M. Han, W. Zhu, Y. Su, S. Angaiah, C. Yan, *Appl. Surf. Sci.* **2020**, *534*, 147644.
[49] H.-C. Chen, Y.-C. Lin, Y.-L. Chen, C.-J. Chen, *ACS Appl. Energy Mater.* **2019**, *2*, 459.
[50] J. Wang, J. Liu, H. Yang, D. Chao, J. Yan, S. V. Savilov, J. Lin, Z. X. Shen, *Nano Energy* **2016**, *20*, 1.
[51] G. Kresse, D. Joubert, *Phys. Rev. B* **1999**, *59*, 1758.
[52] G. Kresse, *Phys Rev B* **1996**, *54*, 11169.
[53] P. E. Blöchl, *Phys. Rev. B* **1994**, *50*, 17953.
[54] J. P. Perdew, K. Burke, *Phys. Rev. Lett.* **1996**, *77*, 3865.
[55] J. P. Perdew, J. A. Chevary, S. H. Vosko, K. A. Jackson, M. R. Pederson, D. J. Singh, C. Fiolhais, *Phys. Rev. B* **1992**, *46*, 6671.
[56] H. J. Monkhorst, J. D. Pack, *Phys. Rev. B* **1976**, *13*, 5188.
[57] G. Henkelman, B. P. Uberuaga, H. Jonsson, *J. Chem. Phys.* **2000**, *113*, 9901.
[58] G. Henkelman, H. Jonsson, *J. Chem. Phys.* **2000**, *113*, 9978.
[59] W. Tang, E. Sanville, G. Henkelman, *J. Phys.: Condens. Matter* **2009**, *21*, 084204.
[60] G. M. Yang, H. Z. Zhang, X. F. Fan, W. T. Zheng, *J. Phys. Chem. C* **2015**, *119*, 6464.

[61] M. Pathak, J. R. Jose, B. Chakraborty, C. S. Rout, *J. Chem. Phys.* **2020**, *152*, 064706.
[62] S. R. KA, A. S. Shajahan, B. Chakraborty, C. S. Rout, *RSC Adv.* **2020**, *10*, 31712.
[63] P. Sun, N. Li, C. Wang, J. Yin, G. Zhao, P. Hou, X. Xu, *J. Power Sources* **2019**, *427*, 56.
[64] X. Feng, J. Ning, D. Wang, J. Zhang, M. Xia, Y. Wang, Y. Hao, *J. Alloys Compd.* **2020**, *816*, 152625.
[65] Y. Lu, M. Zhao, R. Luo, Q. Yu, J. Lv, W. Wang, H. Yan, T. Peng, X. Liu, Y. Luo, *J. Solid State Electrochem.* **2018**, *22*, 657.
[66] B. Huang, J. Yuan, Y. Lu, Y. Zhao, X. Qian, H. Xu, G. He, H. Chen, Available at SSRN: https://ssrn.com/abstract=3983693or.
[67] D. Zhao, M. Dai, H. Liu, K. Chen, X. Zhu, D. Xue, X. Wu, J. Liu, *Adv. Mater. Interfaces* **2019**, *6*, 1901308.
[68] N. Kumar, S. Ghosh, D. Thakur, C.-P. Lee, P. K. Sahoo, *Nanoscale Adv.* **2023**, *5*, 3146.
[69] Z. Li, X. Wang, M. Xu, Z. Yin, J. Zhao, *J. Alloys Compd.* **2022**, *894*, 162492.
[70] J. Huang, J. Wei, Y. Xu, Y. Xiao, Y. Chen, *J. Mater. Chem. A* **2017**, *5*, 23349.
[71] W. Xu, B. Mu, A. Wang, *J. Mater. Sci.* **2018**, *53*, 11659.
[72] R. Gao, Q. Zhang, F. Soyekwo, C. Lin, R. Lv, Y. Qu, M. Chen, A. Zhu, Q. Liu, *Electrochim. Acta* **2017**, *237*, 94.
[73] S. Li, T. Chen, J. Wen, P. Gui, G. Fang, *Nanotechnology* **2017**, *28*, 445407.
[74] H. Wang, Y. Song, J. Zhou, X. Xu, W. Hong, J. Yan, R. Xue, H. Zhao, Y. Liu, J. Gao, *Electrochim. Acta* **2016**, *212*, 775.
[75] R. Thangappan, R. Dhinesh Kumar, R. Jayavel, *J. Energy Storage* **2020**, *27*, 101069.